Inorganic Chemistry
Article

Inorg. Chem. **2009**, *48*, 9693–9699 **9693**
DOI: 10.1021/ic900837r

Multiphase Transformations Controlled by Ostwald's Rule in Nanostructured $Ce_{0.5}Zr_{0.5}O_2$ Powders Prepared by a Modified Pechini Route

Alejandro Várez,[†] Julian Jolly,[†,∥] Patricia Oliete,[‡] Maria Luisa Sanjuán,[‡] Ester García-Gonzalez,[§] Teresa Jardiel,[†] and Jesús Sanz*[,∥]

[†]*Dpto. Materiales, IAAB, Universidad Carlos III de Madrid, 28911 Leganés, Spain,* [‡]*Instituto de Ciencia de Materiales de Aragón, Universidad de Zaragoza-CSIC, Facultad de Ciencias, Universidad de Zaragoza, Spain, 50009, Zaragoza,* [§]*Dpto. Química Inorgánica, Facultad Ciencias Químicas, Universidad Complutense de Madrid, 28040 Madrid, Spain, and* [∥]*Instituto de Ciencia de Materiales de Madrid, CSIC, Cantoblanco, 28049 Madrid, Spain*

Received April 30, 2009

The thermal stability of nanostructured $Ce_{0.5}Zr_{0.5}O_2$ powders prepared by the Pechini method was studied on the nanometric scale by X-ray diffraction (XRD), energy-dispersive spectrometry (EDS), transmission electron microscopy (TEM), nuclear magnetic resonance (NMR), and Raman techniques. Obtained results demonstrate that amorphous powders coming from the thermal decomposition of the precursor transform into the stable crystalline state through one highly disordered and metastable intermediate. This is a new example of successive reactions controlled by Ostwald's rule in inorganic systems. At low calcination temperatures, the combination of Raman spectroscopy, high-resolution electron microscopy, and EDS nanoanalysis showed the formation from the precursor powder of a disordered pseudocubic phase. At 900 °C, metastable T′ and stable T and C phases were detected in XRD patterns. As increasing temperature, crystallites growth and proportions of stable T and C phases increased at the expense of the T′ phase, which completely disappeared at 1300 °C. In analyzed samples, the Raman technique and (crystal by crystal) EDS nanoanalyses were used to detect local phase inhomogeneity. Compositions and relative percentages of phases were investigated by XRD Rietveld analysis and discussed in terms of phase diagrams previously reported.

1. Introduction

Cerium−zirconium mixed oxides have attracted high interest in applications ranging from catalysis[1−4] to fuel cell technologies[5] and solid-state electrolytes.[6] The addition of ZrO_2 to ceria leads to an improvement in ceria oxygen storage capacity (OSC), redox properties, thermal resistance, and low-temperature catalytic activity of oxides.[7−9] These solid solutions have been extensively used in the formulation of modern three-way catalysts for the elimination of contaminant automotive exhaust emissions.[1,2]

Depending on the composition and thermal treatments, three different fluorite-related phases (cubic, monoclinic, and tetragonal) are found in $Ce_xZr_{1-x}O_2$ solid solutions.[1,10] At intermediate compositions (20−80 mol %), the limited solubility of ZrO_2 and CeO_2 accounts for the existence of three types of tetragonal phases, T, T′, and T″, with the same space group $P4_2/nmc$ but different chemical compositions and tetragonal distortion (c/a = 1.02, 1.001−1.02, and 1, respectively).[10] The T phase is stable, while the T′ and T″ phases are metastable. The presence of metastable phases makes difficult the assessment of solid solution ranges in the binary phase diagram.

In the CeO_2−ZrO_2 system, several synthesis routes have been described to obtain homogeneous nanocrystalline solids with high surface areas. In particular, sol−gel,[11] hydrothermal,[12] citrate,[13] and gel combustion[14] methods have been

*To whom correspondence should be addressed. E-mail: jsanz@icmm.csic.es.

(1) Kaspar J.; Fornasiero P. In *Catalysis by Ceria and Related Materials*; Trovarelli, A., Ed.; World Scientific Publishing Company: River Edge, NJ, 2002; Catalytic Science Series, Vol. *2*, Chapter 6, pp 217−241.
(2) Di Monte, R.; Kaspar, J. *J. Mater. Chem.* **2005**, *15*, 633.
(3) Kaspar, J.; Fornasiero, P. *J. Solid State Chem.* **2003**, *171*, 19.
(4) Fornasiero, P.; Di Monte, R.; Ranga Rao, G.; Kaspar, J.; Meriani, S.; Trovarelli, A.; Graziani, M. *J. Catal.* **1995**, *151*, 168.
(5) Steele, B. C. H. *Nature* **1999**, *400*, 619.
(6) Jurado, J. R. *J. Mater. Sci.* **2001**, *36*, 1133.
(7) Hori, C. E.; Permana, H.; Ng, K. Y. S.; Brenner, A.; More, K.; Rahmoeller, K. M.; Belton, D. N. *Appl. Catal., B* **1998**, *16*, 105.
(8) Terribile, D.; Trovarelli, A.; Llorca, J.; de Leitenburg, C.; Dolcetti, G. *Catal. Today* **1998**, *43*, 79.
(9) Putna, E. S.; Bunluesin, T.; Fan, X. L.; Gorte, R. J.; Vohs, J. M.; Lakis, R. E.; Egami, T. *Catal. Today* **1999**, *50*, 343.
(10) Yashima, M.; Takashina, M.; Kakihana, M.; Yoshimura, M. *J. Am. Ceram. Soc.* **1994**, *77*, 1869.
(11) Rossignol, S.; Madier, Y.; Duprez, D. *Catal. Today* **1999**, *50*, 261.
(12) Cabañas, A.; Darr, J. A.; Lester, E.; Poliakoff, M. *J. Mater. Chem.* **2001**, *11*, 561.
(13) Lamas, D. G.; Juarez, R. E.; Lascalea, G. E.; Walsoe de Reca, N. E. *J. Mater. Sci. Lett.* **2001**, *20*, 1447.
(14) Kaspar, J.; Fornasiero, P.; Balducci, G.; Di Monte, R.; Hickey, N.; Sergo, V. *Inorg. Chim. Acta* **2003**, *349*, 217.
(15) Yashima, M.; Arashi, H.; Kakihana, M.; Yoshimura, M. *J. Am. Ceram. Soc.* **1994**, *77*, 1067.

Published on Web 09/11/2009

used. The atomic disorder in nanocrystalline solids complicates their characterization by conventional X-ray diffraction (XRD) techniques. Local structural analysis by high-resolution electron microscopy (HREM) and Raman spectroscopy is required and has been successfully applied to identify the formed phases on nanostructured powders.[15−17]

Amorphous compounds can transform into stable crystalline phases either directly or via intermediate crystalline phases according to Ostwald's rule of stages. This rule states that an unstable system could transform into another transient state, the formation of which is attained by a relatively small free energy loss before reaching the stable state. Recently, the crystallization of amorphous LiFePO_4 has been shown to follow this rule, by direct atomic-level observations with in situ HREM.[18] This result opens a new way to understand the crystallization kinetic pathway in complex inorganic systems.

In the present article, we report the results obtained in the synthesis and characterization of the $Ce_{0.5}Zr_{0.5}O_2$ oxide obtained by use of the Pechini method. This composition was chosen because of its high oxygen storage capacity[19,20] and subsequent interest in heterogeneous catalysis. The characterization of the nanostructured powders has been carried out by means of XRD, transmission electron microscopy (TEM), and X-ray energy dispersive spectroscopy, besides NMR and Raman spectroscopy. This work evidences the importance of performing local structure analysis by techniques such as crystal-by-crystal energy-dispersive spectrometry (EDS) and Raman scattering, especially for low-temperature treated samples, where peak broadening of the X-ray diffractogram can mask small splittings due to symmetry lowering or phase coexistence. Both techniques have been determinant to prove the presence of local deviations from nominal composition, which can serve as nuclei for phase segregation at high temperatures. The obtained results are discussed in terms of the reported CeO_2-ZrO_2 phase diagram and have permitted getting further insight into the understanding of metastability and phase segregation in the $Ce_{0.5}Zr_{0.5}O_2$ phase, in temperature ranges difficult to analyze using standard solid-state reaction methods. The study showed that $Ce_{0.5}Zr_{0.5}O_2$ constitutes one of the few examples of inorganic compounds that follows Ostwald's rule.

2. Experimental Section

2.1. Samples Preparation. Powders of composition $Ce_{0.5}Zr_{0.5}O_2$ were prepared by using polymeric precursors obtained using the Pechini procedure.[21] This method is based on the homogeneous distribution of cations inside a polymeric resin. Since cation dispersion occurs on an atomic scale, powders prepared in this way present high chemical homogeneity. Zirconium(IV) oxide chloride, $ZrOCl_2 \cdot 8H_2O$ (Aldrich, purity of 98%), and cerium hydroxide (Aldrich, purity of 100%) were used as starting reagents. Experimental details are reported in ref 22, where the synthesis of ZrO_2-12 mol % CeO_2 powders for structural ceramic applications was described. The precursor powders obtained with a stoichiometry of $Ce_{0.5}Zr_{0.5}O_2$ were first calcined at 400 °C over 2 h and then heated at different temperatures for 2 h between 600 and 1400 °C.

2.2. Experimental Techniques. Thermogravimetric analyses of polymeric precursors were carried out using a Stanton STA 781-Instrument balance, by heating 300 mg of samples at 10 °C min^{-1} in flowing air (50 mL min^{-1}).

The average composition of samples was determined by EDS X-ray microanalysis performed on a Philips XL30 scanning electron microscope. High-resolution transmission electron microscopy (HRTEM) was performed on a JEOL JEM300FEG microscope equipped with an ISIS 300 X-ray microanalysis system (Oxford Instruments) and a LINK "Pentafet" EDS detector, used in crystal-by-crystal Ce/Zr ratio determinations.

Powder XRD patterns were recorded with Cu Kα1 monochromatic radiation, by using the ($\theta/2\theta$) Bragg−Brentano geometry, on an X'Pert Philips instrument equipped with a curved graphite monochromator. Diffraction patterns were analyzed with the Rietveld method, using the Fullprof program.[23] Prior to structural refinements, pattern matching without a structural model was performed to obtain suitable profile parameters. Then, the structural model was refined by keeping constant profile parameters. In structural models, isotropic atomic displacement parameters were used for Zr, Ce, and O atoms. The fitting process was finished when convergence was reached.

Specific surface areas were determined by N_2 adsorption at 77 K using an ASAP 2010 Micromeritics equipment. Prior to the adsorption experiment, the samples were outgassed at 300 °C for 3 h. The isotherms were analyzed using the Brunauer−Emmett−Teller (BET) model with 0.162 nm^2 as the molecular cross-sectional area for adsorbed nitrogen.

^{1}H magic angle spinning NMR spectra were taken on an MSL 400 Bruker spectrometer working at 400.13 MHz. Samples were spun at 10 kHz around an axis inclined at 54°44′ with respect to the external magnetic field. Spectra were taken after irradiation of the samples with $\pi/2$ pulses of 3 μs (single-pulse technique). The time used between accumulations was 1 s, and the number of scans was 100. Chemical shifts of NMR signals were referred to that of the tetramethylsilane reference.

Room-temperature Raman spectra were recorded on a DILOR XY spectrometer with a liquid-nitrogen-cooled charge-coupled device detector. The excitation was performed through the 50× objective lens of a microscope, using the 514.5 nm line of an Ar laser. The Si mode at 520 cm^{-1} was used for frequency calibration. Lateral spatial resolution was near 2 μm and the spectral line width was ~2 cm^{-1}.

3. Results and Discussion

Samples, initially calcined at 400 °C over 2 h, were first analyzed by XRD and HRTEM (Figure 1). XRD patterns displayed broad peaks characteristic of high surface area amorphous powders (S_{BET} = 78 m^2/g; Figure 1). Small particles of 5 nm average crystal size were observed in HRTEM micrographs. The thermogravimetric (TG) analysis (Figure 2a) of the starting sample displayed three main weight losses between room temperature and 1200 °C. The first one, located between room temperature and 200 °C, has been ascribed to the loss of adsorbed water. The second weight loss, between 200 and 350 °C, corresponds to combustion of the remaining organic matter. The third loss, between 350 and 500 °C, has been attributed to the removal of residual nitrates, as deduced from the evolution of infrared spectra

(16) Zhang, F.; Chen, C.-H.; Hanson, J. C.; Robinson, R. D.; Herman, I. P.; Chan, S.-W. *J. Am. Ceram. Soc.* **2006**, *89*, 1028.
(17) Yeste, M. P.; Hernández, J. C.; Bernal, S.; Blanco, G.; Calvino, J. J.; Pérez-Omil, J. A.; Pintado, J. M. *Chem. Mater.* **2006**, *18*, 2750.
(18) Chung, S.-Y.; Kim, Y.-M.; Kim, J.-G.; Kim, Y.-J. *Nat. Phys.* **2009**, *5*, 68–73.
(19) Vidal, H.; Kaspar, J.; Pijolat, M.; Colon, G.; Bernal, S.; Cordon, A. M.; Perrichon, V.; Fally, F. *Appl. Catal., B* **2000**, *27*, 49.
(20) Fernández-García, M.; Martínez-Arias, A.; Iglesias-Juez, A.; Belver, C.; Hungria, A. B.; Conesa, J. C.; Soria, J. *J. Catal.* **2000**, *194*, 385.
(21) Pechini M. U.S. Patent No. 3,330,697, **1967**.
(22) Quinelato, A. L.; Longo, E.; Leite, E. R.; Bernardi, M. I. B.; Varela, J. A. *J. Mater. Sci.* **2001**, *36*, 3825–3830.
(23) Rodríguez-Carvajal J. *Physica B* **1992**, *192*, 55 (Fullprof Program: Rietveld Pattern Matching Analysis of Powder Patterns, Grenoble, IL, 1990).

with the temperature (not shown). In the sample previously heated at 400 °C, TG losses corresponding to the elimination of nitrates and organic matter were not detected. In both samples, an additional weight loss was observed between 500 and 1200 °C. In order to investigate the nature of the last weight loss, we have recorded at room temperature ^{1}H NMR spectra of samples calcined previously between 400 and 1200 °C (Figure 2b). In all cases, spectra are formed by two components that correspond to OH^- groups of the sample (5 ppm) and proton species of the sample holder used as an internal standard (0 ppm). The intensity of the OH band decreases as the calcination temperature increases. This fact indicates that high-temperature weight losses detected in TG curves correspond to the progressive and irreversible surface dehydroxylation of the sample, which is responsible for the decrease of specific surface area and sintering of nanoparticles.

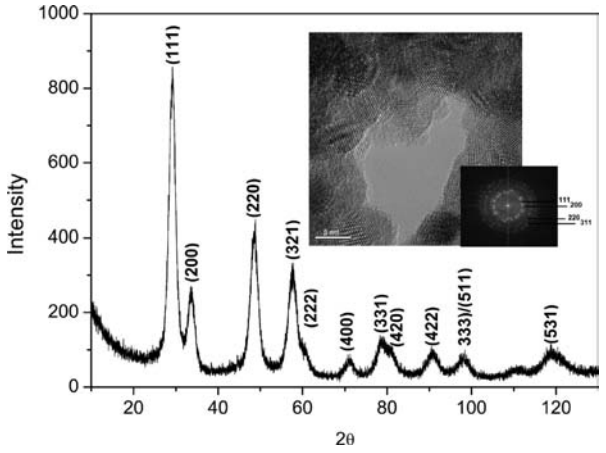

Figure 1. XRD patterns of $Ce_{0.5}Zr_{0.5}O_2$ powders prepared by the Pechini method, after calcination at 400 °C for 2 h. HREM images and the corresponding digital diffraction pattern, given as the inset, illustrate nanoparticle formation.

To study the thermal stability of $Ce_{0.5}Zr_{0.5}O_2$ nanopowders, XRD patterns of samples calcined for 2 h at increasing temperatures were analyzed (Figure 3). In the range 400−900 °C, broad symmetric diffraction maxima, corresponding to nanosized powder samples, were detected (crystal size ranging from 3 to 20 nm). The XRD patterns could be fitted

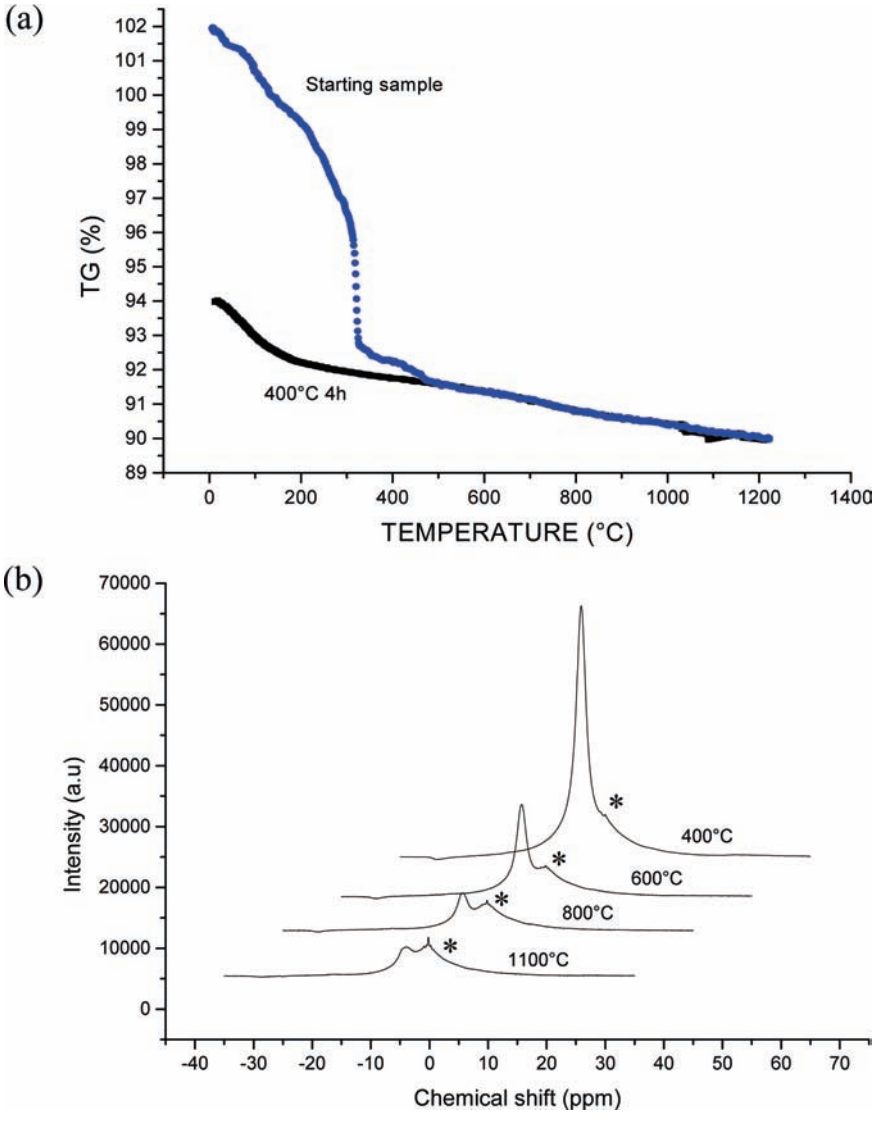

Figure 2. (a) TG profiles of $Ce_{0.5}Zr_{0.5}O_2$ powders obtained from polymer precursors prepared by the Pechini technique, (i) as prepared sample and (ii) after calcination at 400 °C. (b) ^{1}H NMR spectra of samples calcined at different temperatures. The intensity of the NMR signals was normalized with respect to that of the rotor cap (denoted with an asterisk).

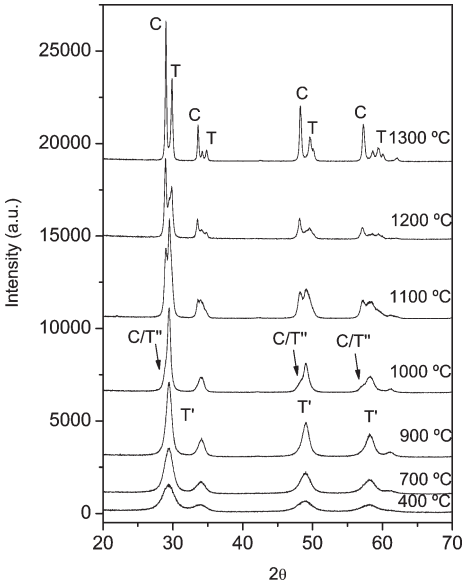

Figure 3. Series of powder XRD patterns of $Ce_{0.5}Zr_{0.5}O_2$ powders calcined (2 h) at different temperatures. At 1000 °C, besides peaks of the tetragonal T′ phase, small shoulders were detected on the left part of the main peaks that were associated with a cubic (or T″) phase. At 1100 °C, the presence of cubic (or T″) and T phases was detected. The proportion of stable phases increases at higher temperatures (1200 °C).

with either the single cubic (space group *Fm*3*m*) or tetragonal (space group $P4_2/nmc$) models reported previously.[10] In both cases, good agreement factors were obtained. Similar broad patterns were found in samples prepared by citrate complexation and microemulsion methods.[24,25] In all cases, the presence of a cubic phase was assumed. At $T \geq 1000$ °C, diffraction maxima become narrower as a consequence of the crystallite size growth detected by HREM. This fact makes it possible to distinguish two different phases with unit cell parameters near those reported for the C/T″ ($x \approx 0.7$ in $Zr_{1-x}Ce_xO_2$ formula) and T′ phases (near the nominal $x \approx 0.5$ composition). Between 1100 and 1200 °C, the presence of a new tetragonal T phase, with a lower Ce content ($x \approx 0.2$), was observed in the XRD patterns. Relative intensities of the C and T phases increase with the temperature at the expense of the T′ phase, which finally disappears at 1300 °C.

The coexistence of three different phases, detected in XRD patterns (C, T, and T′ phases), must be associated with the presence of metastable phases in the binary CeO_2-ZrO_2 system. The formation of metastable crystalline phases from amorphous precursors is often controlled by the empirical Ostwald's rule before the crystallization of thermodynamically stable phases.[18,26] Ostwald proposed that the solid first formed from a melt or solution should be that kinetically more favorable, even if it displays a large Gibbs free energy (not stable polymorph). In nanosized materials, differences in energy of different stable phases decrease considerably when the surface energy is considered.

At increasing temperatures, larger particles are formed and stable phases are developed at the expense of metastable phases. In order to follow the crystallites' growth, HREM images were obtained for samples heated at increasing

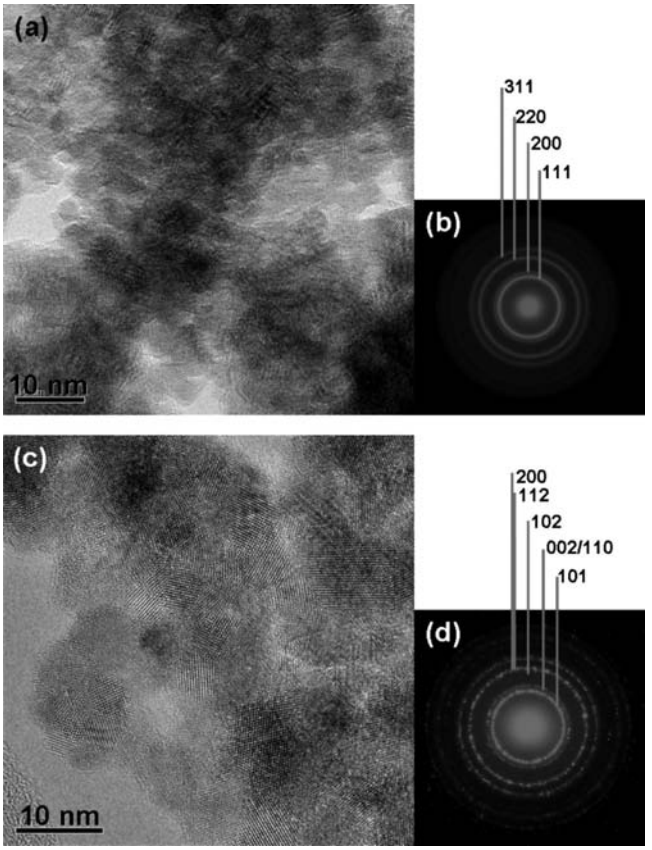

Figure 4. HREM images and corresponding ring diffraction patterns of powders calcined at 400 °C (a and b) and 900 °C (c and d). The diffraction pattern recorded at 400 °C was indexed according to that of the cubic phase (space group: $Pm\bar{3}m$). The diffraction pattern of the sample calcined at 900 °C was indexed according to that of the tetragonal phase (space group $P4_2/ncm$).

temperatures. The sample calcined at 400 °C shows crystallites with a uniform size distribution around 5 nm (Figure 4a). Selected area electron diffraction patterns (Figure 4b) display diffraction rings that can be indexed according to the cubic fluorite structure (space group $Fm\bar{3}m$). The inset of Figure 1 shows a high-resolution micrograph and a digital diffraction pattern (DDP) of this sample. EDS nanoanalyses showed chemical deviations from the nominal composition in the temperature range $400 \leq T \leq 800$ °C. Two types of crystallites (which constitute ~70% of the sample) display compositions close to $Ce_{0.45}Zr_{0.55}O_2$ ($x = 0.45$) and $Ce_{0.6}Zr_{0.4}O_2$ ($x = 0.6$); the rest corresponds to the nominal composition $Ce_{0.5}Zr_{0.5}O_2$ ($x = 0.5$). At 900 °C, the nanostructured character of powders is preserved, the crystal size ranging now between 10 and 20 nm (Figure 4c). Electron diffraction patterns show an extra reflection with respect to the cubic symmetry which has been ascribed to the (102) diffraction ring of the $P4_2/ncm$ tetragonal cell (Figure 4d). Nanoanalyses performed on tetragonal crystals show chemical compositions near $x \approx 0.45$. From 1000 to 1200 °C, the average crystallite size grows above 50 nm and the segregation of phases becomes noticeable. Crystals with compositions near $x = 0.45-0.6$ begin to disappear in parallel with the appearance of two Ce- and Zr-rich phases. At 1100 °C, two different tetragonal phases, with $x \approx 0.45$ (T′ phase) and $x \approx 0.25$ (T phase), were distinguished besides the cubic one ($x \approx 0.8$), the former phase disappearing above 1200 °C (see Table 1 for details). In samples heated at 1200 °C for 2 h, XRD patterns displayed

(24) Kaspar, J.; Fornasiero, P.; Balducci, G.; Di Monte, R.; Hickey, N.; Sergo, V. *Inorg. Chim. Acta* **2003**, *349*, 217.
(25) Vidmar, P.; Fornasiero, P.; Kaspar, J.; Gubitosa, G.; Graziani, M. *J. Catal.* **1997**, *171*, 160.
(26) Threlfall, T. *Org. Proc. Res. Dev.* **2003**, *7*, 1017–1027.

Table 1. Average Particle Size As Deduced from TEM and Chemical Compositions of Nanocrystals As Deduced from EDS and Raman Spectra

T (°C)	average crystal size (nm)	phase composition (Zr/Ce ratio) deduced from EDS nanoanalysis[a]	phases and composition (Zr/Ce ratio) deduced from Raman spectra
400	3−5	(56:44) + (43:57) ∼70%, (50:50) ∼30%	T′ (55:45) + C/T″ (40:60)
700	> 5		
800	∼10		
900	10−20	(56:44) + (46:54) ∼ 75%, (50:50) ∼20%, (25:75) < 5%	T′(55:45), T(∼80:20) + C (≥15:85) (very weak)
1000			T′(60:40), T(∼80:20) + C/T''(15:85)
1100	∼50	(56:44) + (46:54) ∼ 60%, (75:25) ∼ 20%, (22:78) ∼ 20%	T′(65:35), T(∼80:20) + C/T″(20:80)
1200	> 50	(65:35) + (55:45)∼ 50%, (75:25) ∼ 30%, (25:75) ∼ 20%	T′(weak), T(80:20) + C/T″(20:80)
1300	> 100	(75:25) ∼50%, (25:75) ∼50%	T(∼80:20) + C/T″(25:75)
1400	> 100	(80:20) ∼50%, (30:70) ∼50%	T(∼80:20) + C/T″(35:65)

[a] Relative percentages of the different phases as deduced from the observation of a fixed number of crystals.

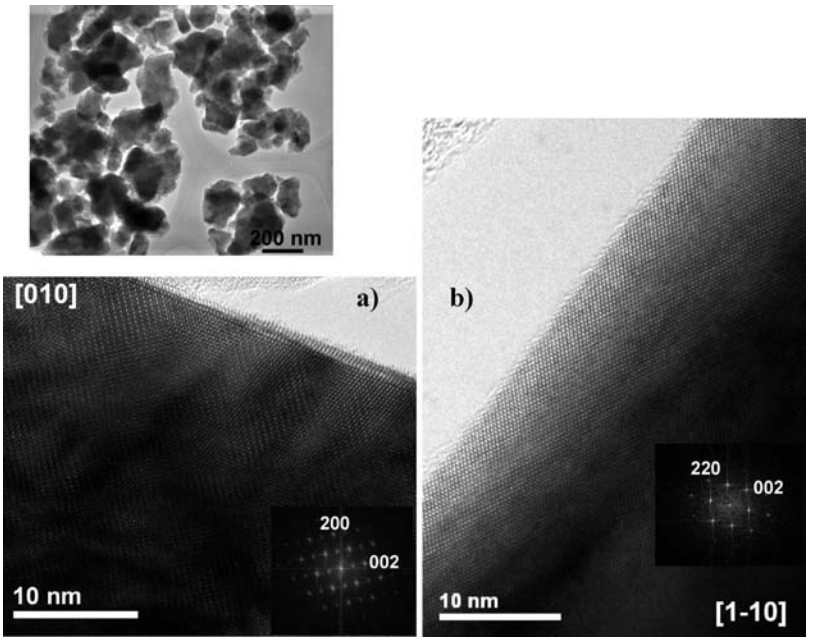

Figure 5. HREM images and electron diffraction (ED) patterns of two crystallites of the sample calcined at 1300 °C, with approximate compositions (a) $Ce_{0.25}Ze_{0.75}O_2$ (tetragonal T phase) and (b) $Ce_{0.75}Zr_{0.25}O_2$ (cubic C phase).

narrow peaks characteristic of samples with a low surface area (S_{BET} = 10 m^2/g).

For calcination temperatures between 1300 and 1400 °C, the average crystallite size grows above 100 nm. Single-crystal electron diffraction and (crystal-by-crystal) EDS analysis show that the sample is mainly constituted by crystallites of two extreme compositions, $x \approx 0.75$ and $x \approx 0.25$, a third group appearing occasionally with $x \approx 0.45-0.55$. Figure 5a shows the high-resolution image of a crystallite with a $Ce_{0.25}Zr_{0.75}O_2$ composition, taken from the sample heated at 1300 °C. The inset displays the corresponding DDP of this crystallite, from which the tetragonal symmetry was deduced. Figure 5b depicts a high-resolution image of a crystal of composition $Ce_{0.75}$-$Zr_{0.25}O_2$ and the corresponding DDP displaying cubic symmetry. In this temperature range, only a few tetragonal crystals with a composition of $Ce_{0.5}Zr_{0.5}O_2$ were detected, suggesting that this phase is not favored at this temperature

The sensitivity of Raman spectroscopy to small oxygen shifts makes it suitable to identify phases in the ZrO_2-CeO_2 system that are, in many cases, difficult to discriminate using XRD. In the cubic CeO_2 phase, only one Raman mode at 465 cm^{-1} is active. In tetragonal T, T′, and T″ phases, with space group $P4_2/nmc$, six modes are expected. Though oxygen atoms occupy the same crystallographic site in the three tetragonal phases, their shifts with respect to the cubic position vary progressively with the Ce content. Accordingly, frequencies and relative intensities of expected modes change considerably with the composition, thus allowing us to discriminate between spectra of T, T′, and T″ phases. In this regard, it should be noted that reference information from samples sintered at high temperatures must be used with caution, since Raman spectra of nanosized samples can differ appreciably from those recorded for well-crystallized samples. In this work, we have used, as a reference, data reported by Yashima et al.[10]

The Raman spectra of samples calcined between 400 and 1400 °C are shown in Figure 6. From 400 to 900 °C, bands are broad and weak, indicating that samples are poorly crystallized. The presence with variable intensity of a band at 190−200 cm^{-1} has been previously attributed to the T′ phase with x = 0.45−0.5. However, both the frequency and the intensity of the pseudocubic phase band appearing at 460−465 cm^{-1} present higher values than that expected for 45−50% Ce samples. This suggests that the spectrum of the T′ phase with $x \sim 0.5$ is superposed on that of a cubic C or pseudocubic T″ phase with $x \approx 0.6-0.65$. This finding agrees with the heterogeneities deduced from the chemical analyses performed on different crystals and stresses the need of using techniques sensitive to local atomic arrangements.

In order to elucidate the possible role of Ce reduction in the formation of metastable phases in nanosized $Ce_{0.5}Zr_{0.5}O_2$, the Raman spectrum in the region of electronic transitions between the low-lying $^2F_{5/2}$ and $^2F_{7/2}$ multiplets of Ce^{3+} (around 2000 cm^{-1}) was systematically investigated. The result was that, within the sensitivity of Raman scattering, no Ce^{3+} was found.

Significant changes occur in spectra of the samples heated above 900 °C. First, the pseudocubic band at ~ 460 cm^{-1} is greatly enhanced as the temperature increases. A deeper analysis of this band shows that between 900 and 1200 °C it consists of two components. The first component at low frequencies ($\nu \approx 453-458$ cm^{-1}) is ascribed to a T′ phase with $x \leq 0.5$, and its intensity decreases upon increasing the treatment temperature. A second very intense component at high frequencies ($\nu \approx 465-480$ cm^{-1}) was attributed to a cubic or pseudocubic Ce-rich phase. At the same time, in the high-frequency wing of the T′ band at 195 cm^{-1}, a new band at $\nu \approx 250$ cm^{-1} was observed, indicating the presence of the so-called T stable phase with low cerium content ($x \leq 0.2$). Thus, we conclude that the segregation of Ce-poor and Ce-rich phases starts at 900−1000 °C, in agreement with HREM and XRD results. These two phases (C/T″ and T) coexist up to 1200 °C with the main T′ phase formed at a low calcination temperature.

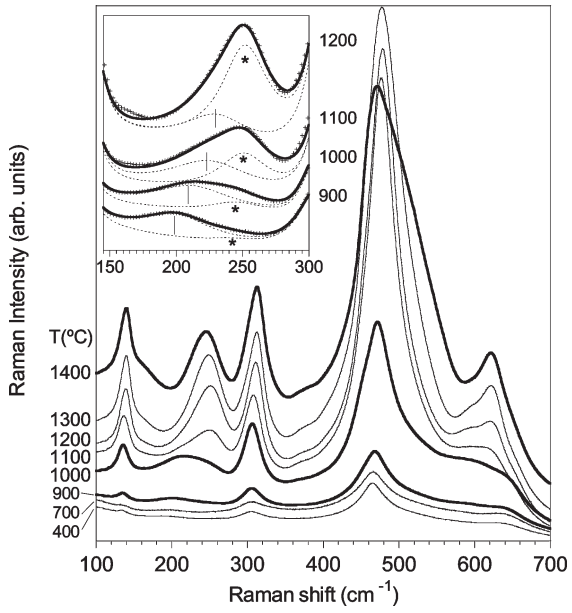

Figure 6. Raman spectra of $Ce_{0.5}Zr_{0.5}O_2$ powders as a function of the calcination temperature. The deconvolution of the region 200−250 cm^{-1} in two bands, assigned to metastable T′ phase (ticks) and stable T phase (asterisks), evidences the onset of the phase segregation above 900 °C (see inset).

As the temperature increases, the three phases evolve in a different way. The position of the T-like band remains almost constant at about 250 cm^{-1}, indicating a fixed Ce content of $x \sim 0.2$. On the other hand, the position of the T′ phase shifts toward a higher frequency, that is, toward lower Ce content. The inset of Figure 6 illustrates the shift of this band from 210 cm^{-1} ($x = 0.4$) at 1000 °C to 225 cm^{-1} ($x = 0.35$) at 1100 °C. In parallel, on increasing the treatment temperature, the pseudocubic band shifts from 467 cm^{-1} at 900 °C, a typical value for a cubic fluorite phase with high cerium content ($x \geq 0.85$), toward higher values, up to $\nu = 479$ cm^{-1} at 1200 °C (T″ phase with $x \approx 0.8$), and then back toward 465 cm^{-1} at 1400 °C, suggesting an evolution of the Ce content with temperature. In fact, the frequency and shape of the pseudocubic band in the spectrum of the sample treated at 1400 °C are characteristic of a T″ phase with $x = 0.65$, just at the border between the T″ and T′ phase domains. The characteristic bands of the T phase were also present.

A more detailed analysis of the XRD patterns by means of the Rietveld method is shown in Table 2. Considering that broad peaks are quite symmetric in the 400−800 °C temperature range, XRD patterns of samples were fitted to a single cubic C phase. Unit cell parameters of this phase practically do not change in this temperature range (a_c = 5.27 Å). The composition of this phase, estimated from unit

Table 2. Structural Parameters Deduced from Rietveld Refinement of the X-Ray Diffraction Patterns for $Ce_{0.5}Zr_{0.5}O_2$ Nanopowders Calcined at Different Temperatures

space group/x		400	600	700	900	1000	1100	1200	1300	1400
	a_t					3.6991(2)	3.7102(1)	3.7014(1)		
	c_t					5.2832(3)	5.2967(2)	5.2975(1)		
	z (O)					0.4554	0.4627	0.4489		
$P4_2/nmc$, T′	Ce (occ)					0.56	0.45	0.45		
	R_B					3.8	3.2	13.2		
	R_F					3.2	2.7	11.4		
	% phase					75(4)	44(2)	29(1)		
	a_t					3.6517(5)	3.6541(2)	3.6469(1)	3.6407(1)	3.6427(1)
	c_t					5.286(7)	5.2566(5)	5.2469(2)	5.2401(1)	5.2407(1)
	z (O)					0.4487(20)	0.4534	0.4695	0.4547	0.4582
$P4_2/nmc$, T	Ce (occ)					0.22	0.20	0.2	0.23	0.20
	R_B					9.8	6.1	13.7	3.7	4.1
	R_F					7.0	4.3	13.9	1.8	1.7
	% phase					0.9(0.1)	26(1)	31(2)	50(2)	43(2)
$Fm\bar{3}m$	a_c	5.2665(2)	5.2665(8)	5.2709(8)	5.2601 (2)	5.3415(2)	5.3462(1)	5.3477(1)	5.3318(1)	5.3121(1)
	Ce (occ)	0.4801	0.4968	0.4800	0.49	0.72	0.74	0.74	0.732	0.622
	R_B	3.1	5.1	6.8	2.7	5.5	4.4	10.6	2.6	2.0
	R_F	2.5	3.4	5.6	1.3	3.8	3.6	6.8	2.0	0.8
	% phase	100	100	100	100	24(1)	30(1)	39(2)	50(2)	57(2)
	R_p	7.1	6.9	10.1	7.2	9.8	10.2	12.2	8.4	10.3
	R_{wp}	9.1	8.9	12.7	9.1	12.6	12.9	15.7	12.0	13.7
	χ^2	1.42	1.48	3.19	1.81	2.52	3.52	2.54	2.37	2.93

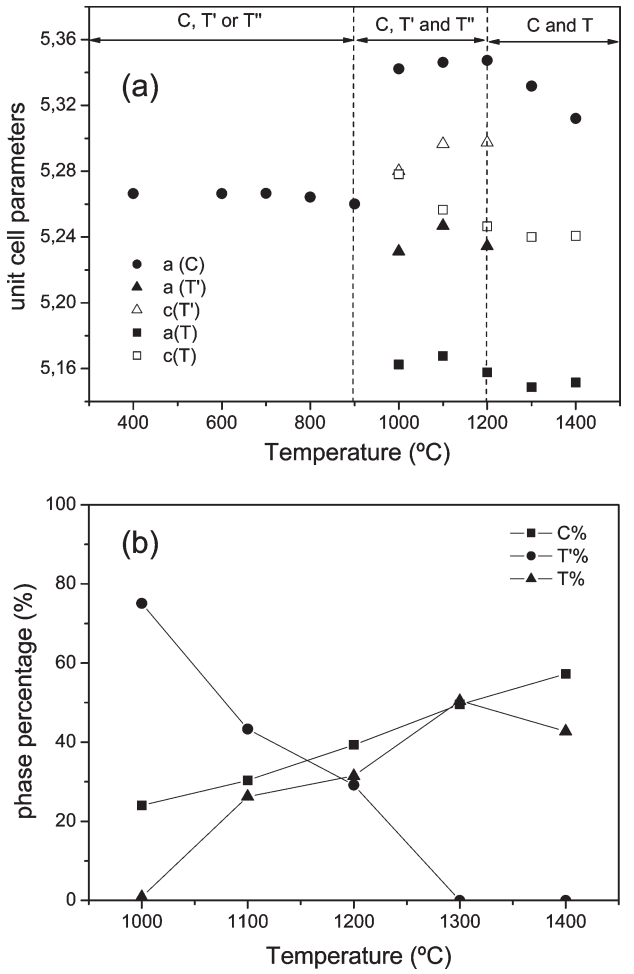

Figure 7. (a) Dependence of lattice parameters of $Ce_{0.5}Zr_{0.5}O_2$ powders on the calcination temperature. Tetragonal unit cell parameters were referred to those of the ideal cubic unit cell. (b) Evolution of the phase percentages of T, T′, and C(T″) phases with the calcination temperature, deduced from the Rietveld refinement of XRD patterns.

cell parameters, was near that deduced from EDS analyses, $Ce_{0.50}Zr_{0.50}O_2$. However, taking into account the local information deduced from Raman and EDS nanoanalysis, some chemical heterogeneity must be present, which is difficult to be deduced using the XRD technique.

Above 900 °C, XRD peaks become narrower, making possible the pattern fitting to three phases. The composition of the cubic phase (C) was near $Ce_{0.72}Zr_{0.28}O_2$, that of the tetragonal T′ phase (c/a = 1.01) was near to $Ce_{0.56}Zr_{0.44}O_2$, while the T phase (c/a = 1.02) displays the $Ce_{0.22}Zr_{0.78}O_2$ composition. As the temperature increases, unit cell parameters of the cubic phase decrease, indicating a slight Ce impoverishment (from 0.72 at 1000 °C to 0.62 at 1400 °C; Figure 7a). In the case of the tetragonal T′ phase, the c/a ratio increases with the calcination temperature from 1.009 at 1000 °C to 1.012 at 1200 °C. In the case of the so-called T-stable phase, the parameters (a and c) remain basically constant between 1100 and 1400 °C. In Figure 7b, the percentage of different phases, deduced from the Rietveld analysis, is given. In agreement with phase diagram predictions,[10] the Ce-poor tetragonal T phase and Ce-rich cubic (C) and pseudocubic (T″) phases grow at the expenses of the metastable T′ phase at increasing temperatures, as deduced from Raman spectra. The decrease of the T phase relative content at 1400 °C is in agreement with the phase diagram and the lever rule, according to which a higher proportion of the Ce-rich phase and, conversely, lower content of the stable T phase must be found on increasing temperature, for a fixed average composition.

4. Conclusions

In this work, the Pechini method has been used to prepare nanostructured $Ce_{0.5}Zr_{0.5}O_2$ materials, with a relatively high surface area (S_{BET} = 78 m^2/g). The combined use of XRD, EDS, TEM, NMR, and Raman techniques has provided a detailed picture of the material on the nanometric scale. At the lowest calcination temperatures, a cubic or pseudocubic phase was found by XRD. However, local structure analysis by EDS and Raman spectroscopy showed that some dispersion around the nominal composition exists, together with local symmetry lowering to T′- or T″-like arrangements. This compositional heterogeneity has been ascribed to the lack of miscibility between Ce and Zr in the reported phase diagram. Above 900 °C, the phase segregation becomes evident. The metastable $Ce_{0.5}Zr_{0.5}O_2$ phase (T′) coexists with two segregated stable phases displaying higher (T″/C) and lower (T) Ce contents in the range of 900−1200 °C. The relative proportion of T + C/T″ phases, deduced by XRD Rietveld analysis, increases at the expenses of the T′ phase at increasing temperatures, this phase disappearing at 1300 °C. The compositional heterogeneity of the low-temperature phase (T′) could help lead to an understanding of the high OSC of these materials and the mechanism of phase segregation, since these regions with lower or higher Ce contents may serve as nuclei for the formation of stable T and C phases, respectively.

The formation of a highly disordered metastable intermediate phase has been interpreted on the basis of Ostwald's rule of successive reactions, in which one (or more) metastable intermediate appears before reaching the equilibrium phases, this case being a new example of an inorganic compound where this empirical rule applies. The obtained results allow one to gain further insight into an understanding of the metastability of the $Ce_{0.5}Zr_{0.5}O_2$ phase. The EDS technique was used to determine the composition of individual particles on the nanoscale level, whereas Raman spectroscopy was used to analyze the structure and composition of detected phases. Within the sensitivity of Raman scttering, no Ce^{3+} was found. Thus, the formation of metastable phases in nanosized systems is ascribed to a surface effect due to either positional or compositional disorder, but not to cerium reduction. The composition and relative amount of stable phases have been discussed in terms of phase diagrams reported previously.

Acknowledgment. We thank the Spanish Agency CICYT (projects MAT2007-64486-C07 and MAT2007-61954) and the regional Government (MATERYENER Program, project S-505/PPQ-0358) for financial support. We thank Prof. A. R. West for encouragement and helpful discussions. Finally, we thank Dr. E. Matesanz for assistance in XRD data collection.